# UC Berkeley

**Title**
Synthesis, Control, and Characterization of Surface Properties of Cu2O Nanostructures

**Permalink**
https://escholarship.org/uc/item/7ph3c605

**Journal**
ACS Nano, 5(5)

**ISSN**
1936-0851

**Authors**
Lee, Sungki
Liang, Chen-Wei
Martin, Lane W

**Publication Date**
2011-05-24

**DOI**
10.1021/nn2001933

Peer reviewed

# Synthesis, Control, and Characterization of Surface Properties of Cu₂O Nanostructures

**Sungki Lee, Chen-Wei Liang, and Lane W. Martin***

Department of Materials Science and Engineering and Frederick Seitz Materials Research Laboratory, University of Illinois, Urbana−Champaign, Urbana, Illinois 61801, United States

Cuprous oxide (Cu₂O) has long been studied because of the unique properties manifested in this material, including the observation of Bose−Einstein condensation of excitons.[1,2] Beyond such basic condensed matter physics studies, there has been considerable attention throughout the years given to Cu₂O (a cubic material with $a = 4.27$ Å and $Pn3m$ symmetry) as a candidate material for photovoltaics[3−6] and photocatalysis[7,8] and even as a negative electrode material for lithium-ion batteries.[9] What has drawn researchers to Cu₂O for such applications are the properties: it is nontoxic, widely abundant, relatively cheap to produce, is a p-type semiconductor with a direct band gap of ∼2.1 eV,[10,11] and it has a maximum theoretical solar conversion efficiency of ∼12% in a single layer photovoltaic cell. Additionally, Cu₂O has a relatively high hole mobility for an oxide material (typically in excess of ∼50 cm²/(V·s) at room temperature) and a large minority carrier diffusion length (∼1 $\mu$m in some cases).[4] More recently, attention has turned to studying the practicality of this material for catalytic systems (especially for water-splitting). As part of this research large surface area samples are required and thus a number of different ways to create nanostructures of this material have been developed, ranging from classic chemical solution approaches (although there are numerous examples from the chemistry world, we focus here on techniques that have demonstrated tunable nanostructure shape evolution[7,12−14]), oxidation by thermal annealing,[15] and growth from the vapor phase, including chemical vapor deposition (CVD)[16] and molecular-beam epitaxy (MBE).[17] Implicit to this research, is the idea that the different surfaces of materials give rise to vastly different properties. In TiO₂, for instance, oxidation mainly occurs on the {001} surfaces and reduction on the {011} surfaces,[18] and for Cu₂O it has been reported that the catalytic activity of Cu₂O nanoparticles is dependent on crystallographic surface orientations.[8]

In this letter, we demonstrate the ability to use epitaxial thin film growth to control the crystallographic surface orientation of Cu₂O nanostructures grown on SrTiO₃ (STO) substrates using pulsed laser deposition (PLD). By fine-tuning the nature of the deposition process, we can deterministically grow high quality, epitaxially oriented nanostructures of Cu₂O with various sizes, densities, and exposed crystal surfaces. We also demonstrate a connection between the adatom energy and flux rate to both the epitaxial relationships and shape of the resulting nanostructures. Furthermore, we present the direct measurement of the surface potentials and electronic structure of the different crystallographic surfaces of Cu₂O through the use of high-resolution

**ABSTRACT** The ability to control nanostructure shape can strongly affect the overall properties of that system. Here we report the ability to deterministically control nanostructure shape, surface facet orientation, and surface potentials of the oxide semiconductor Cu₂O. Epitaxial Cu₂O nanostructures with different shapes and geometries—from boxes to pyramids to huts—have been grown *via* pulsed laser deposition. By varying the adatom energy and flux per laser pulse we can tune the nature of the nanostructure geometry, the total density of features, the relative surface area to volume ratio, and can create polar, nonequilibrium surfaces. In addition to detailed structural analysis of the nanostructures, high-resolution Kelvin probe force microscopy has been used to systematically analyze the surface potential and electronic structure of the (100), (110), and (111) surfaces of Cu₂O. These studies suggest that each surface, possessing a unique atomic structure, gives rise to different surface energy levels of conduction and valence bands and the formation of electronic surface junctions. The implication of these findings in terms of a range of applications is discussed.

**KEYWORDS:** Cu₂O · Kelvin probe force microscopy · pulsed laser deposition · surface properties · epitaxy
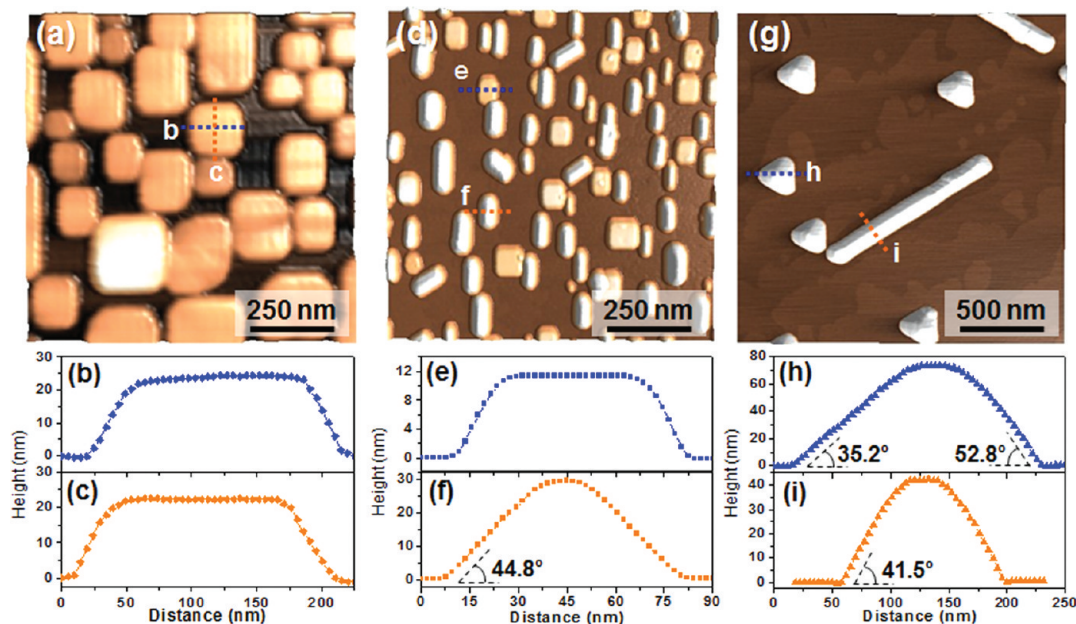
**Figure 1.** High resolution AFM images and corresponding line-traces completed at the dashed lines for Cu$_2$O nanostructures on STO (001) (a–c), STO (110) (d–f), and STO (111) (g–i) substrates. Important angles are shown where appropriate.

Kelvin probe force microscopy (KPFM) and provide two-dimensional surface potential maps of electronic surface junctions thought to be of great importance for a range of applications. These experiments allow us to construct a proposed energy band diagram for the various surfaces of the Cu$_2$O nanostructures and provide insight into future device structures based on this material.

## RESULTS AND DISCUSSION

Cu$_2$O nanostructures were synthesized by PLD and characterized by a variety of techniques, details of which are provided in the Methods section. Additional details concerning the effect of varying a wide range of variables during the growth process of these nanostructures are provided in the Supporting Information. Observation of the Cu$_2$O nanostructures following growth with atomic force microscopy (AFM) reveals that the nanostructures directly mimic the crystallographic symmetry of the underlying substrate (Figure 1). Square or rectangular nanostructures with flat-top, plateau-like structures (Figure 1a) and sides parallel to the edges of the substrate (100 and 010) were observed on STO (001) substrates. Line-traces across the nanostructures (Figure 1b,c) confirm the plateau-shape with abrupt step-edges. On STO (110) two different rectangular nanostructures were observed with either flat-top, plateau-like, or hut-like angled surface geometries (Figure 1d). Although the majority of these features are found to be oriented with the long-axis of the nanostructure along the (1$\bar{1}$0) of the substrate, we have observed a small fraction that have the long axis aligned along the [001]. Line-traces across the short axis of such plateau-like nanostructures (Figure 1e)

reveal similar structure to those grown on STO (001). Line-traces across the hut-like nanostructures (Figure 1f) reveal a symmetric, angled structure with an angle between the (110) substrate surface and the surface of the nanostructure of 44.75 ± 0.75°. (All angles are the result of statistical analysis of a large number of nanostructures, at different locations on a given substrate, and across at least 5–10 different samples. Additional details concerning the measurement of these features is provided in the Supporting Information.) Finally, two types of nanostructures are observed on STO (111) substrates. The first possesses a triangular pyramid shape, and all triangular features are found to point along the ⟨1$\bar{1}$0⟩ of the substrate. The second type of nanostructure found on STO (111) substrates possesses a long, rectangular structure with a hut-like, angled surface (similar to those observed on STO (110)) and are found to have their long axis aligned along the ⟨11$\bar{2}$⟩ of the substrate, with no observed preference for a specific ⟨11$\bar{2}$⟩ direction (we note that across these samples three variants of such nanostructures are observed). Line-traces of the triangular pyramid nanostructures were done along all three equivalent directions of the feature, a sample of which is shown in Figure 1h. From close inspection of scanning electron microscopy (SEM) and AFM images, it is found that these nanostructures are actually triangular pyramids, with truncated edges and tops. The line-trace in Figure 1h goes across one of the truncated edges, across the apex, and down the flat side of the nanostructure. Such a line-trace gives rise to two important angles. First, the angle between the (111) surface of the substrate and the truncated edge of the pyramid which is found to be 35.2 ± 0.82° and second, the
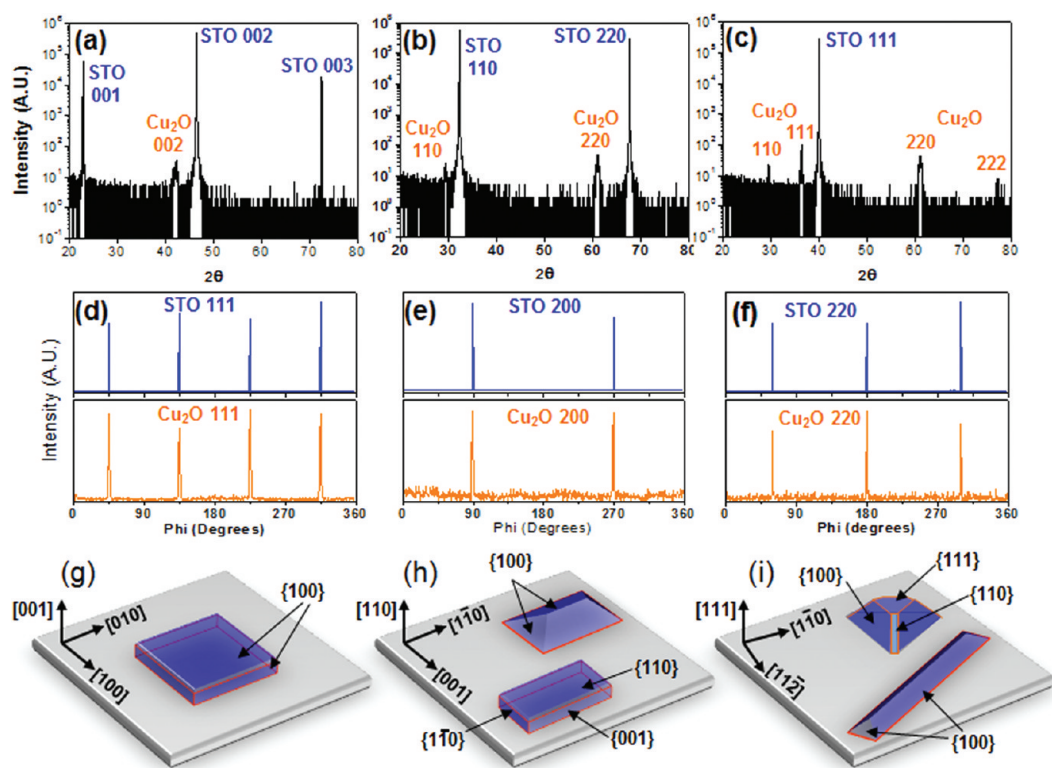
**Figure 2.** Wide angle $\theta-2\theta$ X-ray diffraction scans of $Cu_2O$ nanostructures on (a) STO (001), (b) STO (110), and (c) STO (111) substrates. Corresponding in-plane epitaxy was determined from $\varphi$-scans on (d) STO (001), (e) STO (110), and (f) STO (111) substrates. Corresponding schematic illustration of nanostructure shape and epitaxy on (g) STO (001), (h) STO (110), and (i) STO (111) substrates.

angle between the (111) surface of the substrate and the flat facet of the nanostructure which is found to be 52.8 ± 4.6°. Likewise, line-traces completed on the hut-like nanostructures (Figure 1i) reveal symmetric features with an angle between the (111) substrate surface and the facets of the nanostructure to be 41.5 ± 2.2°.

Structural analysis and determination of epitaxial relationships was completed using X-ray diffraction (Figure 2). $\theta-2\theta$ scans of nanostructures grown on STO (001), (110), and (111) substrates reveal that the structures are single phase, possessing no evidence of CuO or other impurity phases. Additionally, nanostructures grown on STO (001) and (110) substrates were found to grow epitaxially, possessing only 00*l* (Figure 2a) and *hh*0 (Figure 2b) diffraction peaks, respectively. Nanostructures grown on STO (111) substrates were found to possess diffraction peaks corresponding to *hh*0 and *hhh* diffraction conditions (Figure 2c). The triangular pyramid structures observed in Figure 1g correspond to nanostructures with (111) orientation, and the long, rectangular hut-like structures correspond to (110) oriented features. Furthermore, $\varphi$-scan studies revealed in-plane epitaxial relationships of $(100)_{Cu_2O}//(100)_{STO}$ and $(010)_{Cu_2O}//(010)_{STO}$ (Figure 2d), $(001)_{Cu_2O}//(001)_{STO}$ and $(1\bar{1}0)_{Cu_2O}//(1\bar{1}0)_{STO}$ (partial data shown in Figure 2e), and $(1\bar{1}0)_{Cu_2O}//(1\bar{1}0)_{STO}$ and $(11\bar{2})_{Cu_2O}//(11\bar{2})_{STO}$ (partial data

shown in Figure 2f) for $Cu_2O$ nanostructures on STO (001), (110), and (111) substrates, respectively.

Combining these X-ray diffraction results with the previous angle analysis from the AFM line traces, we can produce a full crystallographic picture of the nanostructures. On STO (001) substrates, the plateau-like nanostructures grow (001) oriented and are made up entirely of {100} surfaces (Figure 2g), a result that has never been reported for nanostructures grown from the vapor phase. On STO (110) substrates, all nanostructures grow (110) oriented, and for the plateau-like nanostructures the top surface is a {110} surface and the sides are a combination of two {001} and two {1$\bar{1}$0} surfaces, while for the hut-like nanostructures the sides are {001} surfaces (Figure 2h). Finally, the triangular pyramid nanostructures on STO (111) grow (111) oriented; the truncated edges of the nanostructure are {110}-type; the flat, side-surfaces of the pyramid are {100}-type; and the top surface is {111}-type (Figure 2i). Finally, the hut-like nanostructures, which grow (110) oriented, have {100}-type side surfaces (Figure 2i).

These observations are quite different from the findings reported previously for the epitaxial growth of $Cu_2O$ nanostructures. Specifically growth on both STO (001)[19,20] and LaAlO$_3$ (001)[21] revealed the formation of square pyramidal shapes possessing {111} crystal facets that grew rotated by 45° with respect
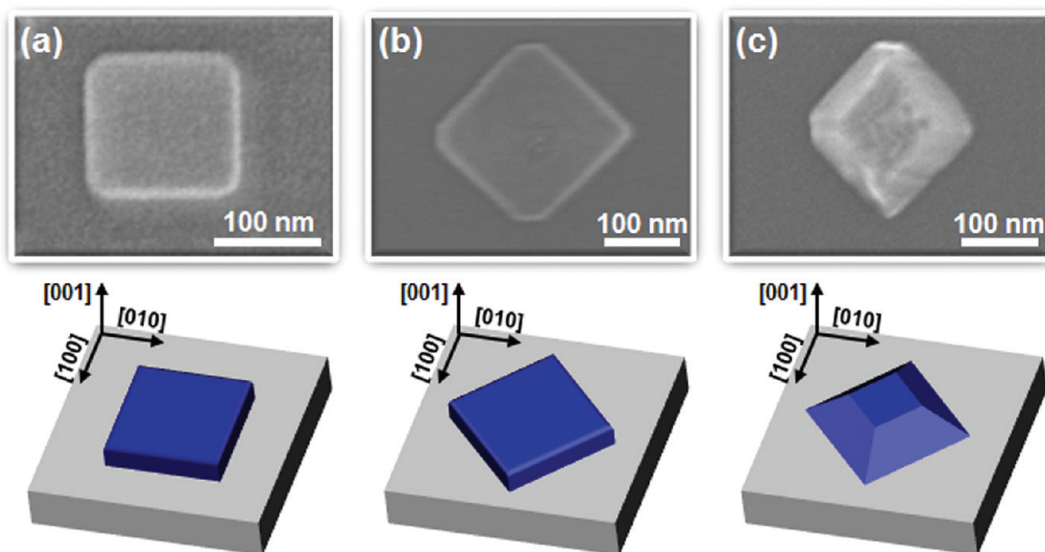
**Figure 3.** SEM images of typical nanostructure geometry on STO (001) substrates at 700 °C and a corresponding illustration of the typical nanostructure geometry as a function of laser fluence; (a) 0.78, (b) 0.59, and (c) 0.39 J/cm$^2$.

to the underlying substrate crystal lattice (similar results were also observed on MgO (110)[16]). In the current work, however, the $Cu_2O$ nanostructures are found to directly map out the underlying crystallographic nature of the substrate and possess decidedly different crystal shapes. Additionally, observations from previous results had suggested that the {111} $Cu_2O$ surface should have considerably lower surface energy than the {100} surface (we note that more recent density functional theory (DFT) calculations further suggest that the {111} surface has lower energy than both the {100} and {110} surfaces).[8] In the current work, however, we observe many nanostructures possessing highly polar {100} and {110} surfaces contrary to previous results. What is clear is that the growth of these nanostructures is strongly influenced by the deposition process, which can be used to effectively tune the nature of nanostructure epitaxy and shape of the nanostructures.

As part of this study we have investigated the effect of a number of growth parameters on the nanostructure growth. For instance, substrate orientation is found to effect the density of nanostructures with growth on STO (111) producing significantly lower densities, but larger average volume nanostructures. At the same time, growth temperature is also found to greatly impact the evolution of these nanostructures. Specifically as the temperature is increased, the density of nanostructures decreases and the average volume of a given nanofeature increases, suggesting that the increased temperature greatly enhances the adatom mobility on the surface and enhances growth at the expense of nucleation. A detailed account of these effects can be found in the Supporting Information. However, the variable found to have the largest effect on the nanostructure growth was laser fluence. Fixing

the growth temperature at 700 °C we have varied the laser fluence from 0.78 (Figure 3a) to 0.59 (Figure 3b) and 0.39 J/cm$^2$ (Figure 3c) and have observed marked changes in the nanostructure shape and epitaxy on STO (001) substrates. In all cases, the resulting nanostructures are (001) out-of-plane oriented. Samples grown at the highest energy (Figure 3a) give rise to plateau-like nanostructures with the nanostructure edges aligned parallel to the ⟨100⟩ of the STO (001) substrate. Decreasing the laser fluence by ∼25% results in plateau-like nanostructures that are rotated by 45° relative to the underlying substrate (Figure 3b). Finally, by further decreasing the laser fluence to half the original value, we obtained square pyramid (and truncated pyramid) nanostructures that are rotated 45° relative to the underlying substrate (Figure 3c). These nanostructures possess {111} crystal side surfaces and {001} top surfaces and are consistent with the features previously observed in a number of publications.[16,19,21,22]

Both this and previously published work suggests that coherent nanoisland formation occurs for $Cu_2O$ on a number of substrates. To date this fact has been explained as being the result of large lattice mismatch. Current theories suggest that the stress generated at the coherent epitaxial interface must be accommodated *via* 3D island growth[16] and strain relaxation in $Cu_2O$ is thought to be similar to that observed for Ge on Si.[23] Furthermore, most reports have observed a 45° rotation of the nanostructures relative to the underlying substrate. On the basis of lattice mismatch alone, one would expect cube-on-cube growth (for example) in $Cu_2O$ on MgO (001); however, this is not the case. This stems from the fact that the oxygen sublattice of $Cu_2O$ is bcc while that of MgO (or any of the perovskites) is fcc. This means that a cube-on-cube alignment would place Cu ions adjacent to Mg and

O ions alternately, thereby creating a strong electrostatic repulsion when the Cu and Mg ions are aligned, thereby driving a 45° rotation of the lattice.[24]

The differences observed in this manuscript can be condensed down to two points: different nanostructure shapes and epitaxial relationships are observed in nanostructures grown *via* PLD. Both of these features can be tuned by changing the laser fluence and thus this suggests that both the enhanced adatom kinetic energy associated with PLD and enhanced materials flux rate at the surface can help the system overcome the energy barriers for creating high-energy, polar surfaces and unfavorable in-plane epitaxy. In fact, the average kinetic energy of an incident species arriving at the substrate in PLD can be as high as 1−100 eV while the incident energy of an adatom from a thermal deposition process, such as molecular beam epitaxy, is on the order of 0.1−1 eV.[25,26] Previous studies have focused on the growth of $Cu_2O$ nanostructures *via* CVD[16,21] and MBE,[19,20] where both have low adatom kinetic energies (0.1−1 eV) and reported flux rates of between 0.36 and 1.8 Å/min and in all instances observed square pyramid structures rotated by 45° in-plane relative to the substrate lattice. Although the measurement and calculation of adatom energies in PLD can be cumbersome, on the basis of data available in the literature[27−29] we estimate that laser fluences of 0.78 and 0.59 $J/cm^2$ correspond to adatom energies in excess of 1 eV and a laser fluence of 0.39 $J/cm^2$ corresponds to an adatom energy of ∼0.5 eV. Additionally our flux rates for the samples in Figure 3 range from ∼0.4 to 4 Å/min, and only when both the adatom energy and flux rate was brought down to levels consistent with the previous reports did the nanostructures take on the commonly observed geometries (Figure 3c). We also note that changing repetition rate of the laser alone did not result in the same effects as observed when laser fluence was changed. This further suggests that the dose per pulse and the energy of the species in that pulse are key in determining the final shape and epitaxy of the nanostructures.

Such fine-level control of the nanostructure shape could be essential for optimizing future devices based on $Cu_2O$. Devices that aim to take advantage of the electronic properties of such oxide semiconductors can be dramatically influenced by changes in surface properties and electronic structure. One such example is the use of $Cu_2O$ as a photocatalyst for oxidation/reduction of $H_2O$. Such processes have been found to be largely dependent on not only the type but also the ratio and location of the various crystallographic surfaces present.[8] Empirical observations of different reaction rates and first-generation DFT models suggest the importance of the surface properties of this material in determining functionality; however, no measurements of the differences in electronic structure of these surfaces have been undertaken until now. To do

this, we have utilized KPFM,[30] a scanning-probe-based technique that allows us to measure the surface potential difference between the scanning probe tip and the sample surface and to construct a 2D map of the surface potential of the $Cu_2O$ nanostructures. Such a technique allows for the direct comparison of electronic structure of the (001), (110), and (111) surfaces. We focus here on the study of nanostructures on STO (111) substrates which have been shown to possess two features: triangular pyramid nanostructures possessing all three surfaces and hut-like nanostructures with (100) and (110) surfaces.

High-resolution AFM images (not shown) and corresponding AFM amplitude images (note that amplitude measures the voltage difference between the measured amplitude on the detector in the AFM and the amplitude set-point and is an effective derivative of the height image, thus providing information about regions of constant slope on the surface) (Figure 4a,d) of the hut-like and triangular pyramid nanostructures reveal the presence of two and three different surfaces, respectively. Focusing first on the KPFM analysis of the hut-like $Cu_2O$ nanostructures, a map of the KPFM potential (Figure 4b) and the KPFM potential overlaid on the height (Figure 4c) reveals that the highest potentials are observed on the {100} surfaces and intermediate potentials are observed on the {110} surfaces. Turning our attention to the triangular pyramids, again the highest surface potentials are observed on the highly polar {001} surfaces, intermediate potentials on the {110} surfaces, and the lowest potential on the {111} surface (Figure 4e,f). On the basis of our analysis of over 15 different samples and many more nanostructures, we have found that these surface potential values correspond to −530, −465, and −450 mV, relative to the Pt-coated tips used in this study, for the {100}, {110}, and {111} surfaces, respectively. Again, we observe a difference between {001} and {111} surfaces of ∼80 mV. To our knowledge, this is the first direct measurement of the surface potential difference of the various crystallographic faces of $Cu_2O$.

To determine the electronic structure of $Cu_2O$, we have undertaken a careful set of experiments meant to overcome the sometimes qualitative nature of KPFM. It is widely known that the data collected from the KPFM can be convoluted with information about the surface potential, trapped surface charges, and measurement artifacts among other things, including considerable dependence on the tip conditions. This traditionally makes it difficult to be quantitative and to correlate (with any accuracy) the measured surface potential values with the work function of the material. To work around these limitations and provide a semiquantitative band diagram for $Cu_2O$, we have utilized a range of known and previously measured reference samples (that is, Au and STO) and have worked to carefully cross-correlate the data collected from the KPFM with
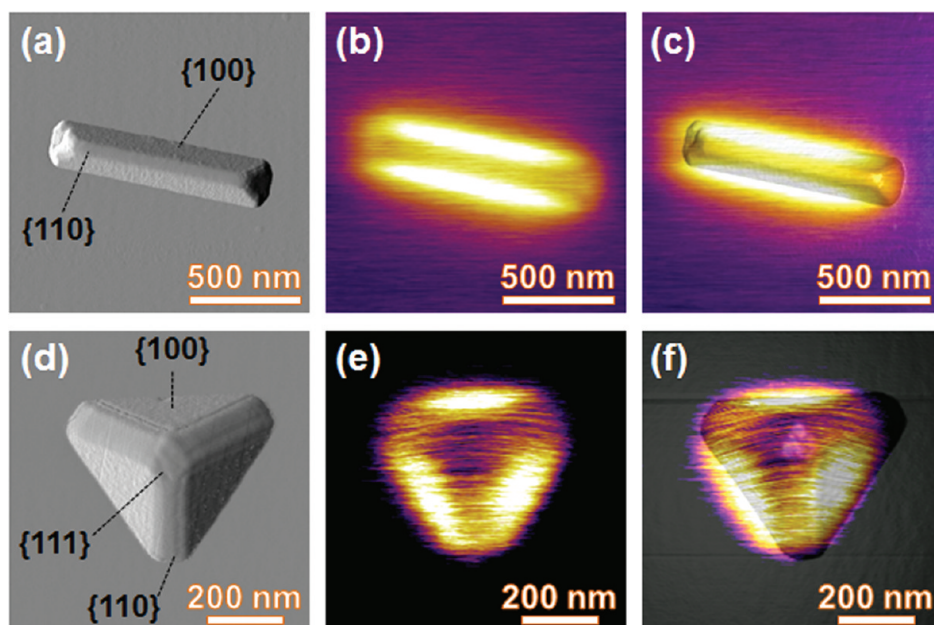
**Figure 4.** KPFM studies of hut-like and triangular pyramid nanostructures on STO (111) substrates: (a and d) AFM amplitude images showing surface topography, (b and e) KPFM surface potential images, and (c and f) surface potential superimposed on amplitude images for hut-like and triangular pyramid nanostructures, respectively.
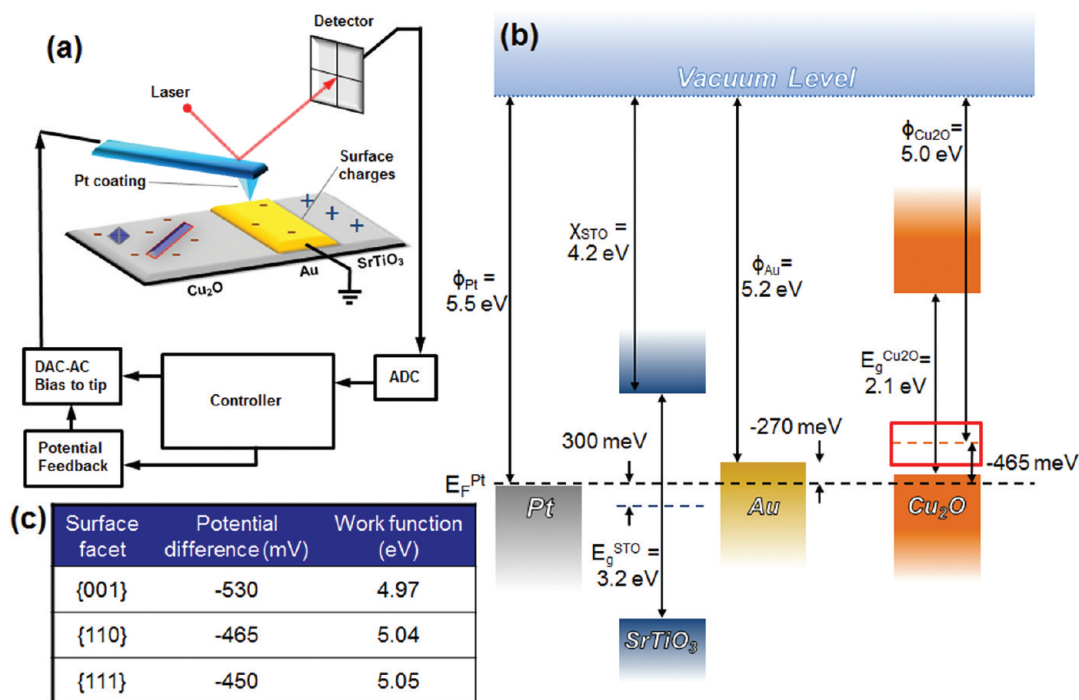


| Surface facet | Potential difference (mV) | Work function (eV) |
|---|---|---|
| {001} | -530 | 4.97 |
| {110} | -465 | 5.04 |
| {111} | -450 | 5.05 |

**Figure 5.** (a) Illustration of the experimental setup used to provide quasi-quantitative surface potential/work function values. (b) Proposed energy band diagram of $Cu_2O$ and reference samples. $\phi$, $\chi$, and $E_F$ represent work function, electron affinity, and Fermi energy values, respectively. (c) Table summarizing differences in electronic structure for the various $Cu_2O$ surfaces.

previously measured work functions and electron affinities. To do this, we have studied model systems, such as that shown schematically in Figure 5a. To begin, we have examined the interaction between the Pt-coated scanning-probe tips used here with a number of reference samples: STO (001) and (111) substrates and electron-beam evaporated, grounded Au thin

films. We observe an offset of 300 mV between the Pt-coated tip and the as-received STO substrates and an offset of −270 mV between the Pt-coated tip and the grounded Au thin films. Assuming an electron affinity for the STO substrate of 4.1 eV,[31] we obtain a work function for the Pt of 5.5 eV. It should be noted that this is a very reasonable number and falls into the

middle of the measured range for Pt (5.12–5.93 eV).[32] With this number set, we can examine the offset with the Au thin films which are found to possess a work function of ~5.2 eV; again consistent with previously measured values between 5.1 and 5.47 eV.[28] We note that these surface potential values for STO and Au are generally consistent to within 10–20 mV for all new tips (values are observed to drift as the scanning-probe tips wear with use). We have observed that the surface potential difference between the tip and the sample surface changes sign when the tip is severely damaged or worn-out (there is a Cr under-layer (with work function ~4.5 eV)[32] used as an adhesion layer between the Si tip and the Pt coating) and this can be used as an immediate check of the accuracy and status of the measurement. We have undergone considerable effort to understand the factors that affect the KPFM data acquisition and have settled on an optimal retraction height (*i.e.,* the distance between the tip and the sample surface, set to 50 nm for all measurements reported here) as well as the appropriate power/integral gain in the KPFM feedback loop. With these parameters held constant, we have gone on to probe systems possessing grounded Au, STO, and $Cu_2O$ features with the same tips (Figure 5a). The cross correlation of data and statistical analysis of the various surface potentials allow us to make a semiquantitative assessment of the work function of the $Cu_2O$ nanostructures. A schematic energy diagram from this data is provided (Figure 5b). From our analysis, we obtain an average work function for the $Cu_2O$ of 5.0 eV with additional small deviations in work function for each of the surfaces studied. A detailed description of the various $Cu_2O$ surfaces is given in Figure 5c.

## CONCLUSIONS

The implications of these observations are quite dramatic. The presence of such differences in electronic structure of the various facets of $Cu_2O$ can give rise to exciting effects, including effective electronic surface junctions between facets. Such features could be important for a range of technologies from oxide electronics to photocatalytic systems. For instance, in $TiO_2$ it has been observed that oxidation and reduction of $H_2O$ occur predominantly on the {001} and {011} surfaces and, on the basis of computational approaches, it has been suggested that this occurs because the valence band of $TiO_2$ (001) extends to somewhat higher energies as compared to the (101) surface.[33] The difference

in energy levels between crystal faces can drive electrons and holes to different faces. By understanding the surface potential of all the possible facets of $Cu_2O$ and developing fine-level control of the types of faces present in these materials, we can engineer an optimum feature for enhanced charge separation. Previous DFT studies[8] of the $Cu_2O$ system suggested that the valence band of the $Cu_2O$ {100} and {110} surfaces extend to higher energies relative to the {111} surfaces. The predicted energy differences in these studies were a very small fraction of an eV. Our results are consistent with these calculations as we have measured the valence band edge of the {100} to be higher than that of the {110} and that higher than the {111} surface. In the current work we have observed a difference in surface potential between {100} and {111} $Cu_2O$ surfaces of nearly 80 mV. This surface potential difference could, in turn, lead to the formation of an electronic surface junction that can drive charge separation at these surfaces more effectively. From these analyses, it is thought that the photogenerated holes on the {111} facets will be transferred to the {100} and {110} facets and, in turn, electrons will be transferred to the {111} facets. In the context of an application such as photocatalysis, this would mean that the primary sites for oxidation would be on {100} and {110} facets and for reduction on {111} facets. Thus in an attempt to optimize such a surface junction, one would want to engineer structures possessing mixtures of {100} and {111} surfaces to enhance these effects. Furthermore, the algorithm used here to analyze $Cu_2O$ could be applied to many different materials and could provide additional insight into the complex problems occurring in such systems in applications such as electronics, photovoltaics, photocatalysis, and beyond.

In conclusion, we have used epitaxial growth *via* PLD to gain deterministic control over the shape, volume, density, and surface structure of $Cu_2O$ nanostructures. By varying the thin film growth process, especially the adatom energy (*via* laser fluence), we have established a pathway to tune the nature of nanostructure geometry in this exciting material. Using KPFM we have also measured the surface potential difference between three common crystal facets of $Cu_2O$ and have constructed a schematic energy diagram to describe the system. Armed with knowledge, researchers could open up new pathways to the study of exotic exciton and photocatalytic behavior in these materials and could drive enhancements of these effects.

## METHODS

$Cu_2O$ nanostructures were synthesized by PLD in an on-axis geometry using a KrF excimer laser ($\lambda$ = 248 nm) from a cupric oxide (CuO) ceramic target (Praxair, 99.995%). Nanostructures, have been grown on a variety of substrates, but here we focus

on growth on single-crystal STO (001), (110), and (111) substrates. Growth temperatures were varied from 650 to 750 °C, and the nanostructures were grown and cooled in 1 mTorr of oxygen (this oxygen pressure was selected after referring to the copper–oxygen phase diagram).[34] Unless otherwise noted,

each set of nanostructures was grown using 840 pulses of the laser (7 min at 2 Hz). The structural nature of the nanostructures was probed using four-circle X-ray diffraction (Philips X'pert MRD-Pro) and field-emission scanning electron microscopy (SEM, Hitachi S-4800 high resolution SEM operated at 15 kV). Tapping-mode atomic force microscopy (AFM) was used to study the surface morphology of the nanostructures. We note that angles between crystallographic facets of the $Cu_2O$ nanostructures and the surface of the substrate reported here are statistical averages from a large number of measurements. The tips used in this study allow for accurate measurement and mapping of features making an angle upward of ~70° to the surface. Features inclined to angles greater than this will appear broadened due to the geometry of the scanning probe tip. The average radius of the tips used in this study is between 10 and 20 nm and have a cone angle of 40°. KPFM studies were done using Pt-coated tips including ElectriTap190-G and ElectriTap300-G (Budget Sensors), NSC35 (Mikromasch), and NCHPt (Nanosensors) and were completed at a constant height of 50 nm following an initial height image in tapping mode. All scanning probe studies were undertaken in an Asylum MFP-3D system.

## REFERENCES AND NOTES

1. Lin, J. L.; Wolfe, J. P. Bose−Einstein Condensation of Paraexcitons in Stressed $Cu_2O$. *Phys. Rev. Lett.* **1993,** *71*, 1222–1225.
2. Snoke, D. W. Spontaneous Bose Coherence of Excitons and Polaritons. *Science* **2002,** *298*, 1368–1372.
3. Rai, B. P. $Cu_2O$ Solar Cells: A Review. *Sol. Cell.* **1988,** *25*, 265–272.
4. Mittiga, A.; Salza, E.; Sarto, F.; Tucci, M.; Vasanthi, R. Heterojunction Solar Cell with 2% Efficiency Based on a $Cu_2O$ Substrate. *Appl. Phys. Lett.* **2006,** *88*, 163502.
5. Darvish, D. S.; Atwater, H. A. Modeling, Synthesis, and Characterization of Thin Film Copper Oxide Solar Cells, from the Photovoltaics Specialists Conference (PVSC), 2009 34th IEEE, 7−12 June 2009, pp 2195−2199, doi: 10.1109/PVSC.2009.5411394.
6. Lee, Y. S.; Bertoni, M.; Chan, M. K.; Cedar, G.; Buonassisi, T. Earth Abundant Materials for High Efficiency Heterojunction Thin Film Solar Cells, from the Photovoltaics Specialists Conference (PVSC), 2009 34th IEEE, 7−12 June 2009, 2375−2377, doi: 10.1109/PVSC.2009.5411314.
7. Xu, H.; Wang, W.; Zhu, W. Shape Evolution and Size Controllable Synthesis of $Cu_2O$ Octahedra and Their Morphology-Dependent Photocatalytic Properties. *J. Phys. Chem. B* **2006,** *110*, 13829–13834.
8. Zheng, Z.; Huang, B.; Wang, Z.; Guo, M.; Qin, X.; Zhang, X.; Wang, P.; Dai, Y. Crystal Faces of $Cu_2O$ and Their Stabilities in Photocatalytic Reactions. *J. Phys. Chem. C* **2009,** *113*, 14448–14453.
9. Poizot, P.; Laruelle, S.; Grugeon, S.; Dupont, L.; Tarascon, J.-M. Nanosized Transition-Metal Oxides as Negative Electrode Materials for Lithium Ion Batteries. *Nature* **2000,** *407*, 496–499.
10. Pollack, G. P.; Trivich, D. Photoelectric Properties of Cuprous Oxide. *J. Appl. Phys.* **1975,** *46*, 163–172.
11. Akimoto, K.; Ishizuka, S.; Yanagita, M.; Nawa, Y.; Paul, G. K.; Sakurai, T. Thin Film Deposition of $Cu_2O$ and Applications for Solar Cells. *Solar Energy* **2006,** *80*, 715–722.
12. Siegfried, M. J.; Choi, K.-S. Elucidating the Effect of Additives on the Growth and Stability of $Cu_2O$ Surfaces *via* Shape Transformation of Pregrown Crystals. *J. Am. Chem. Soc.* **2006,** *128*, 10356–10357.
13. Ng, C. H. B.; Fan, W. Y. Shape Evolution of $Cu_2O$ Nanostructures *via* Kinetic and Thermodynamic Controlled Growth. *J. Phys. Chem. B* **2006,** *110*, 20801–20807.

14. Kuo, C.-H.; Huang, M. H. Facile Synthesis of $Cu_2O$ Nanocrystals with Systematic Shape Evolution from Cubic to Octahedral Structures. *J. Phys. Chem. C* **2008,** *112*, 18355–18360.
15. Zhou, G.; Yang, J. C. Formation of Quasi-one-dimensional $Cu_2O$ Structures by *in Situ* Oxidation of Cu(100). *Phys. Rev. Lett.* **2002,** *89*, 106101.
16. Markworth, P. R.; Liu, X.; Dai, J. Y.; Fan, W.; Marks, T. J.; Chang, R. P. H. Coherent Island Formation of $Cu_2O$ Films Grown by Chemical Vapor Deposition on MgO (110). *J. Mater. Res.* **2001,** *16*, 2408–2414.
17. Du, Y.; Atha, S.; Hull, R.; Groves, J. F.; Lyubinetsky, I.; Baer, D. R. Focused-Ion-Beam Directed Self-Assembly of $Cu_2O$ Islands on $SrTiO_3$ (100). *Appl. Phys. Lett.* **2004,** *84*, 5213–5215.
18. Ohno, T.; Sarukawa, K.; Matsumura, M. Crystal Faces of Rutile and Anatase $TiO_2$ Particles and Their Roles in Photocatalytic Reactions. *New J. Chem.* **2002,** *26*, 1167–1170.
19. Lyubinetsky, I.; Lea, A. S.; Thevuthasan, S.; Baer, D. R. Formation of Epitaxial Oxide Nanodots on Oxide Substrate: $Cu_2O$ on $SrTiO_3$ (100). *Surf. Sci.* **2005,** *589*, 120–128.
20. Kuchibhatla, S. V. N. T.; Hu, S. Y.; Yu, Z. Q.; Shutthanandan, V.; Li, Y. L.; Nachimuthu, P.; Jiang, W.; Thevuthasan, S.; Henager, C. H., Jr.; Sundaram, S. K. Morphology, Orientation Relationship, and Stability Analysis of $Cu_2O$ Nanoclusters on $SrTiO_3$ (100). *Appl. Phys. Lett.* **2009,** *95*, 053111.
21. Zhang, H.; Goodner, D. M.; Bedzyk, M. J.; Marks, T. J.; Chang, P. R. H. Formation and Kinetics Study of Cuprous Oxide Nanodots on $LaAlO_3$ (001). *Chem. Phys. Lett.* **2004,** *395*, 296–301.
22. Yu, Z. Q.; Yang, C. M.; Engelhard, M. H.; Nachimuthu, P.; McCready, D. E.; Lyubinetsky, I. V.; Thevuthasan, S. Epitaxial Growth and Microstructure of $Cu_2O$ Nanoparticle/Thin Films on $SrTiO_3$ (100). *Nanotechnology* **2007,** *18*, 115601.
23. Floro, J. A.; Chason, E.; Freund, L. B.; Twesten, R. D.; Hwang, R. Q.; Lucadamo, G. A. Evolution of Coherent Islands in $Si_{1-x}Ge_x$/Si(001). *Phys. Rev. B* **1999,** *59*, 1990–1998.
24. Kawaguchi, K.; Kita, R.; Nishiyama, N.; Morishita, T. Molecular Beam Epitaxy Growth of CuO and $Cu_2O$ Films With Controlling the Oxygen Content by the Flux Ratio of Cu/$O^+$. *J. Cryst. Growth* **1994,** *143*, 221–226.
25. Willmott, P. R.; Huber, J. R. Pulsed Laser Vaporization and Deposition. *Rev. Mod. Phys.* **2000,** *72*, 315–328.
26. Shin, B.; Leonard, J. P.; McCamy, J. W.; Aziz, M. J. Comparison of Morphology Evolution of Ge (001) Homoepitaxial Films Grown by Pulsed Laser Deposition and Molecular Beam Epitaxy. *Appl. Phys. Lett.* **2005,** *87*, 181916.
27. Franghiadakis, Y.; Fotakis, C.; Tzanetakis, P. Energy Distribution of Ions Produced by Excimer-Laser Ablation of Solid and Molten Targets. *Appl. Phys. A: Mater. Sci. Process.* **1999,** *68*, 391–397.
28. Harilal, S. S.; Bindhu, C. V.; Tillack, M. S.; Najmabadi, F.; Gaeris, A. C. Internal Structure and Expansion Dynamics of Laser Ablation Plumes into Ambient Gases. *J. Appl. Phys.* **2003,** *93*, 2380–2388.
29. Geohegan, D. B. Spectroscopic and Ion Probe Characterization of Laser Produced Plasmas Used for Thin Film Growth. *Laser Ablation: Mechanisms and Applications*; Miller, J. C., Haglund, R. F., Jr., Eds.; Springer-Verlag: Heidelberg, Germany, 1991; pp 28−37.
30. Palermo, V.; Palma, M.; Samori, P. Electronic Characterization of Organic Thin Films by Kelvin Probe Force Microscopy. *Adv. Mater.* **2006,** *18*, 145–164.
31. Chung, Y.; Weissbard, W. B. Surface Spectroscopy Studies of the $SrTiO_3$ (100) Surface and the Platinum-$SrTiO_3$ (100) Interface. *Phys. Rev. B* **1979,** *20*, 3456–3461.
32. Michaelson, H. B. The Work Function of the Elements and its Periodicity. *J. Appl. Phys.* **1997,** *48*, 4729–4733.
33. Gong, X. Q.; Selloni, A. Reactivity of Anatase $TiO_2$ Nanoparticles: The Role of the Minority (001) Surface. *J. Phys. Chem B* **2005,** *109*, 19560–19562.
34. Ogale, S. B.; Bilurkar, P. G.; Mate, N.; Kanetkar, S. M.; Parikh, N.; Patnaik, B. Deposition of Copper Oxide Thin Films on Different Substrates by Pulsed Excimer Laser Ablation. *J. Appl. Phys.* **1992,** *72*, 3765–3769.